

EDINBURGH
INSTRUMENTS



PRECISION RAMAN

Best-in-class Raman microscopes
for research and analytical requirements
backed with world-class customer
support and service.



edinst.com

RESEARCH ARTICLE

The presence of superoxide ions and related dioxygen species in zinc oxide—A structural characterization by *in situ* Raman spectroscopy

Dieter Fischer¹  | Dejan Zagorac² | J. Christian Schön¹¹Max Planck Institute for Solid State Research, Stuttgart, Germany²Institute of Nuclear Sciences Vinca, Materials Science Laboratory, University of Belgrade, Belgrade, Serbia**Correspondence**Dieter Fischer, Max Planck Institute for Solid State Research, Heisenbergstr. 1, 70569, Stuttgart, Germany.
Email: d.fischer@fkf.mpg.de**Funding information**

Ministry of Education, Science, and Technological Development of Serbia, Grant/Award Number: 1702201

Abstract

Zinc oxide exhibits unique properties that are reflected in a wide variety of applications, particularly in the field of transparent, conductive films. However, less attention has been paid to their color. Here, we present the synthesis of yellow-gray ZnO films at room temperature by femtosecond pulsed laser deposition. *In situ* Raman investigations of these polycrystalline ZnO films reveal the existence of superoxide ions, O_2^- , in zinc oxide, which are responsible for the yellow color, and are also detected in ZnO powder and single crystals. In addition, further dioxygen species are identified in the samples, including the O_2 -molecule. The negative charge excess caused by the dioxygen species creates metallic zinc as a byproduct. Structural analysis reveals an unforced realization of the dioxygen species in the ZnO lattice. Density functional theory (DFT) calculations support the assumed structural displacements as well as the observed, unexpected Raman bands. These results open up completely new insights into the behavior of ZnO.

KEYWORDS

Raman spectroscopy, solid-state-structures, superoxide ion, thin films, zinc oxide

1 | INTRODUCTION

Zinc oxide is an extensively studied compound, but in many of these studies,^[1] little attention has been paid to the color of ZnO. There is a wide range of colors reported for ZnO independent of the form of the solid. In nature, ZnO occurs as the mineral zincite in the colors yellow, light-green, and red, which is commonly ascribed to impurities such as Fe and Mn.^[2] ZnO powder is mainly synthesized by dehydration of zinc hydroxide that yields white pure material.^[3] Commercially available powder generally has a slight pale-yellow hue. In addition, the powder is thermochromic and reversibly changes its color to yellow

with temperature in air, which is explained by the loss of oxygen at high temperatures, for example, at 800°C.^[4]

Most single crystals of ZnO are grown by hydrothermal processes in alkali-metal hydroxide fluxes.^[5,6] The crystals obtained exhibit colors ranging from yellow, green, and red to brown. The origin of these colors is explained by impurities (Li, Na, K, H, Fe, etc.) introduced into the crystals from fluxes or by the apparatus materials used.^[5] The commercial high-quality crystals, for example, for substrates, are light yellow. Additionally, structural investigations suggest that the different colors are related to the oxygen content of the crystals.^[7] Annealing of ZnO crystals in zinc vapor changes the color from light

This is an open access article under the terms of the [Creative Commons Attribution](https://creativecommons.org/licenses/by/4.0/) License, which permits use, distribution and reproduction in any medium, provided the original work is properly cited.

© 2022 The Authors. *Journal of Raman Spectroscopy* published by John Wiley & Sons Ltd.

yellow to dark red, which is explained by removal of zinc vacancies and introduction of oxygen vacancies.^[8] In contrast, highly crystalline ZnO films ($\leq 4 \mu\text{m}$ thick) grown by liquid phase epitaxy on substrates appear completely transparent and colorless.^[9] These results and their explanations are not consistent and require a more detailed investigation of the origin of the color.

In reports of the deposition of ZnO films on substrates by sputtering,^[10] pulsed laser deposition (PLD),^[11] chemical vapor deposition,^[10,12] and molecular beam epitaxy,^[13] the films obtained are generally described as transparent, without any mentioning of colors. The transmittance of the films is generally above 80%. Sometimes the films exhibit reduced transparencies,^[14,15] and, to the best of our knowledge, only in one case amorphous brown-colored films are described.^[16] However, the color is a very important property, especially with regard to the application as transparent, conductive (n-type) oxide coatings. Furthermore, from a scientific point of view, it is necessary to understand the origin of the color. This raises the question: Are all (pure) crystalline ZnO films colorless, or are there also colored ZnO films? The deposition of films via the gas phase enables optimal avoidance of impurities and allows to focus on the structural arrangement of zinc and oxygen. Therefore, we deposit ZnO films using the femtosecond-PLD^[17] and characterize the properties of these films, in particular to obtain indications of color, using X-ray diffraction and Raman spectroscopy. The thickness of these films is set just below 100 nm, which represents the optimum for solar cell applications.^[18]

2 | MATERIALS AND METHODS

2.1 | Chemicals

ZnO powder (99.999%, lightly yellow) was purchased from Acros Organics (Geel, Belgium) and the ZnO crystals (oriented (001) and (100)) from the CrysTec GmbH (Berlin, Germany). The PLD target was generated by pressing the ZnO powder with 8 tons pressure in argon atmosphere using a hydraulic press (Perkin Elmer, Germany), forming a round disc with a diameter of 16 mm and a thickness of 4–5 mm. After pressing, the disc showed a more intense yellow color, compared to the powder, together with a slightly gray surface, which suggests a loss of oxygen on the surface forming metallic zinc.

2.2 | Synthesis

Film depositions were performed using a femtosecond laser system (FemtoRegen, High-Q-Laser GmbH,

Austria) with a wavelength of 516 nm at 442 femtosecond (pulse length) focused (0.05 mm) on the PLD-target surface with a power of 50–70 mW (energy per pulse of 0.05–0.07 mJ at 1 kHz). The ablation operated with a line scan of 50 mm/s on the rotating target (0.125 rpm) in a vacuum chamber with a process pressure of $6\text{--}8 \times 10^{-8}$ mbar for a period of 6–7 h per sample; further details in Fischer et al.^[19] The ZnO was deposited on single-crystal sapphire substrates (orientation (0001), CrysTec GmbH, Germany) at 25°C, which were clamped on a copper holder and subsequently transferred to an X-ray diffractometer while maintaining vacuum. During the process some macroscopic particles were also deposited onto the substrate. This phenomenon is well known for the ablation with laser pulses in the nanosecond/picosecond range and also occurs in a reduced manner for our laser system with a pulse length of about 0.5 ps. Generally, the ablation and deposition of large particles is not significant for the femtosecond-PLD.^[20]

To avoid contamination of ZnO (forming, e.g., hydroxides and carbonates) the complete handling—starting from the preparation of the target, the deposition, characterization, and the storing of the samples—was performed in argon atmosphere or under high vacuum.

2.3 | X-ray diffraction

X-ray powder diffraction was measured by a θ/θ -diffractometer (D8-Advance, Bruker AXS, Germany) with a Goebel mirror (Cu-K α radiation) inside a vacuum chamber (1×10^{-7} mbar) in reflection mode. The powder patterns were monitored at an angle of incidence of 10° using an area sensitive detector (Vantec-500, Bruker AXS). The structure refinement of the integrated patterns was performed by the Rietveld method via the TOPAS software (TOPAS Vers. 4.2, Bruker AXS). For the visualization of the crystal structures the software package Diamond version 4.4.1 (Crystal Impact GbR, Bonn, Germany) was used.

2.4 | *In situ* Raman spectroscopy

The X-ray diffractometer was equipped with a laser-microscope Raman spectrometer (BXFM microscope and iHR 550 spectrometer, Horiba, Germany) operating with a 532-nm laser and a Peltier-cooled CCD camera (Synapse). The resolution of the spectrometer (three-grating 1800 L/mm) was 1 wavenumber (cm^{-1}), and the measurements were started at 90 cm^{-1} . The laser beam (20 mW) was focused with an objective (100 \times , 0.9 NA) on the samples inside a vacuum chamber

(1×10^{-7} mbar) using a confocal aperture in quasi-backscattering geometry. The direct coupled laser beam passed through a window in the vacuum chamber and finally impinged on the samples (see Figure S1). Subsequently, the Raman signal was coupled by a fiber-optic cable to the spectrometer. Thus, the Raman spectra were recorded *in situ* while maintaining vacuum and temperature of the prepared ZnO films. Laser irradiation caused a local heating of the samples, which initiated the ordering inside the obtained macroscopic particles. Since the temperature caused by the irradiation could not be measured directly, we used the results of an investigation on doped ZnO samples^[21] with comparable experimental conditions as an indication of the temperature present in our investigation. Thus, the temperature reached was estimated to be below 700°C based on experiments on doped ZnO samples^[21] with similar laser power. In addition, an increase of the intensity of Raman bands, accompanied by broadening and red-shift, have been observed with increasing laser power, but no change in the ZnO structure^[21] was seen. The Raman spectra of the ZnO powder and crystals were measured with the same apparatus.

2.5 | Scanning electron microscopy

The scanning electron microscopy (SEM) images were recorded with a field emission microscope (Merlin, Zeiss GmbH, Germany) using an accelerating voltage of 5 kV and an in-lens detector. The samples were transferred into the microscope in an argon atmosphere using a custom-built transfer chamber.

2.6 | DFT calculations

The investigated ZnO structures were generated using $2 \times 2 \times 2$ ZnO wurtzite supercells, where one oxygen ion is replaced by a dioxygen species and where one oxygen atom is moved from a regular occupied tetrahedral position to an inverse tetrahedral void (cf. structural considerations). The *ab initio* calculations were performed using the CRYSTAL17 code, based on the linear combination of atomic orbitals.^[22] The local optimizations of structures employed analytical gradients, and the subsequent phonon calculations were based on analytical first and numerical second derivatives.^[23] Structural relaxations for various charged states of dioxygen species in ZnO have been performed followed by phonon calculations at the Γ -point for a neutral cell. The LO-TO splitting at the Γ -point was calculated within the framework of the coupled perturbed Kohn–Sham method.^[24]

Structure optimizations were performed on the density functional theory (DFT) level, employing the B3LYP functional (Becke's three parameter functional in combination with the correlation functional of Lee, Yang, and Parr)^[25] and the generalized gradient approximation (GGA) with the PBE (Perdew, Burke, and Ernzerhof) functional.^[26] Each local optimization employed an all-electron basis set (AEBS): a [6s5p2d] basis set in the case of zinc, and a [4s3p] basis set in the case of oxygen.^[27] Structural and crystallographic analysis has been performed using the KPLOT software package.^[28]

3 | RESULTS AND DISCUSSION

3.1 | Experiments

In our experiments, ZnO is deposited on sapphire substrates at room temperature under a high vacuum. Film thicknesses range between 60 and 100 nm. The ZnO films obtained are yellow-gray in color. Figure 1a depicts a sample on a transparent sapphire substrate photographed on a white background. The corresponding SEM images (Figure 1b,c) reveal rough, dense films showing a granular surface structure with particle sizes between 10 and 70 nm. In addition, a few macroscopic particles per $(100 \mu\text{m})^2$ are visible with sizes of 0.5–5 μm , formed by the PLD-process. The X-ray powder diffraction pattern of deposited films in Figure 1e shows the expected reflections of the wurtzite structure of ZnO^[29] accompanied by additional weak broad reflections of metallic zinc. The deposited ZnO films are polycrystalline and consist of ZnO with about 20 wt% zinc. The refined crystal sizes are 36 nm (ZnO) and 8 nm (Zn); compare Rietveld data: Table S1. Both components are expected to contribute to the color of the films. Thus, the yellow-gray color of the films is a result of a mixture of gray zinc and yellow ZnO as discussed below, and is comparable to the yellow single crystals of ZnO (see Figure 1d).

Raman spectra of the deposited ZnO films give more insights into the local ordering. These measurements reveal unexpected results. Six Raman-active phonon modes exist for the ZnO lattice: at 99 and 438 cm^{-1} (E_2 , most intensive), at 378 and 574 cm^{-1} (A_1), and at 410 and 590 cm^{-1} (E_1)^[30] (see Table 1). These modes are clearly visible in the measured spectra of our purchased powder, ZnO single crystals, and the PLD target used (pressed from powder); see Figure 2a. However, none of these specific modes are visible in the Raman spectra of our films. These spectra exhibit a very broad band from 300 to 600 cm^{-1} (oxygen-related wavenumbers) along with an increasing ramp up to 100 cm^{-1} (zinc-related wavenumbers); see Figure 2b. The broad band shows a

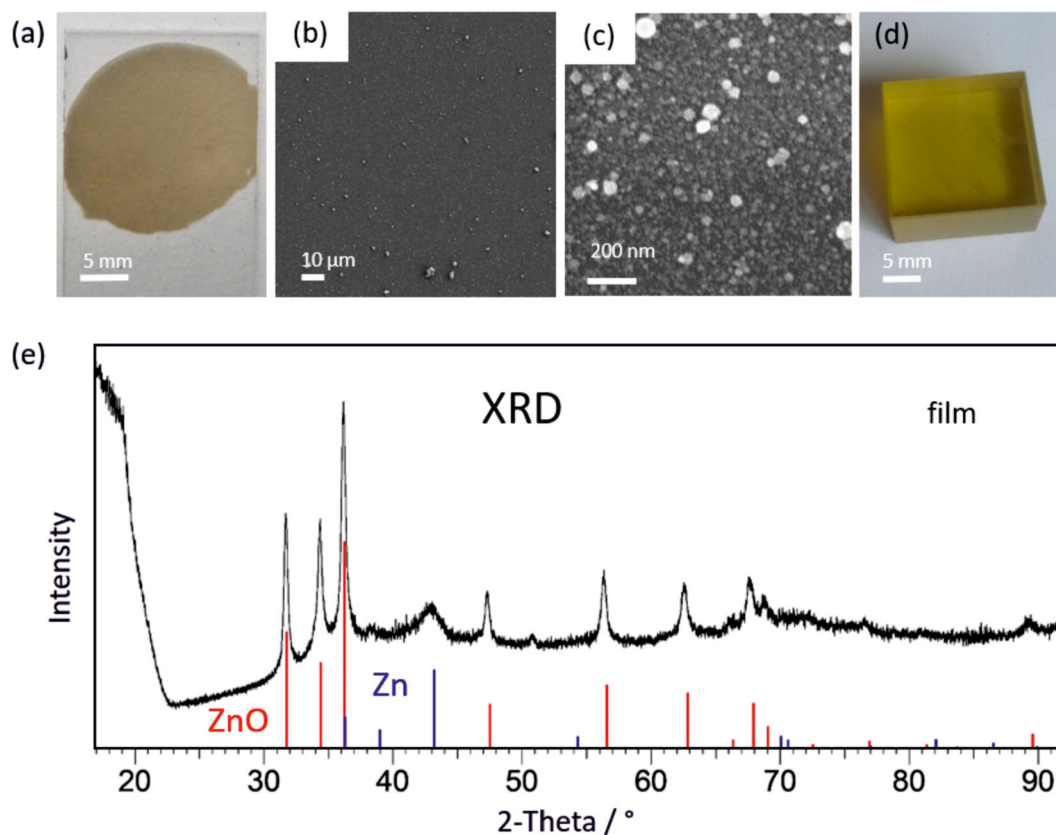


FIGURE 1 (a) Photograph of a deposited ZnO film on a transparent sapphire substrate (sample diameter ~ 20 mm). (b,c) Scanning electron microscopy (SEM) images of ZnO films (two magnifications). (d) Single crystal of ZnO ($21 \times 21 \times 11$ mm³). (e) X-ray powder pattern of a ZnO film (line pattern of wurtzite ZnO structure (red), of metallic Zn (blue)) [Colour figure can be viewed at wileyonlinelibrary.com]

maximum at ~ 555 cm⁻¹ and a shoulder at ~ 440 cm⁻¹. Additionally, a slowly increasing intensity ramp of the spectra starting from 800 to ~ 1600 cm⁻¹ is remarkable. The Raman intensity in this range varies slightly from sample to sample and gives hints of bands at ~ 1140 , 1360, and 1570 cm⁻¹. No further bands are detectable for higher wavenumber up to 3700 cm⁻¹ (see Figure S2). The total disagreement of these Raman spectra with the Raman bands of ZnO is completely unexpected. These results suggest an extremely distorted lattice in the deposited films. We believe that this anomalous behavior is due to the formation of dioxygen species such as superoxide ions, O₂⁻, in the zinc oxide samples, which is also responsible for the yellow color.

3.2 | Structural considerations

The wurtzite crystal structure of ZnO consists of ZnO₄ and OZn₄ tetrahedra as shown in Figure 3a with Zn–O and O–O distances of 198 and 321 pm,^[29] respectively. In other words, the zinc atoms form a hexagonal close

packing where oxygen atoms occupy one half of the tetrahedral voids, which are all corner-connected; the remaining unoccupied tetrahedral voids also form a separate corner-connected network. Thus, two types of tetrahedral voids exist: one where the top of the tetrahedra is directed down along the *c*-axis (chosen as normal occupied orientation) or up (inverse, empty orientation), as illustrated in Figure 3b by the blue and yellow tetrahedra for oxygen. These tetrahedra appear in face-connected pairs—with each pair effectively forming a trigonal bipyramid of Zn atoms—and by occupying both neighbor tetrahedra (red-colored oxygen atoms in Figure 3b), the formation of dioxygen species with an interatomic distance of 123 pm occurs, which corresponds to the distance in the O₂-molecule of 121 pm.^[31] With a shift of the *z*-value of oxygen (the only adjustable site parameter of the wurtzite structure) from *z* = 0.382 (common value in ZnO) to *z* = 0.375 (value for the ideal wurtzite structure)^[32] the O–O distance increases to 130 pm. This value agrees well with the oxygen distances of the yellow superoxide ion O₂⁻ of 128 to 137 pm in alkali-metal and tetraorganylammonium superoxides.^[33,34] Additionally, the

TABLE 1 Measured Raman wavenumbers (in cm^{-1}) of our ZnO samples along with assignments (gray shaded: the six Raman-active phonon modes of ZnO, yellow shaded: wavenumbers/wavenumber range associated with superoxide ions) and calculated wavenumbers of ZnO structures with different oxygen position as well as observed bulk ZnO Raman data

| Assignment | Experimental data (this study) | | | | | Calculated data (B3LYP) | | | | | ZnO data ³⁰ |
|--------------------------|--------------------------------|---------------------|---------------|---------------|---------------------|-------------------------|--|-----------------|-----------------|-------------------------|--|
| | Film | Particle irradiated | Crystal (001) | Crystal (100) | Powder (PLD target) | Powder (PLD target) | Oxygen z = 0.38 | Oxygen z = 0.42 | Oxygen z = 0.50 | Crystal | |
| E_2 low | 100–280 235 sh | 97 | 97 | 97 | 97 | 100 | 110 | 117 | 103 | 99 | E_2 low |
| Zn–Zn disorder | 100–280 240 sh | 200 | 201 | 201 | 199 | 200 | | | | 203 | $2E_2$ low, 2TA |
| | 328 | 331 | 330 | 328 | 329 | | | | | 333 | E_2 high- E_2 low |
| $A_1(\text{TO})$ | 376 | 376 | 376 | 374 | 377 | | 376 | 137 | 0 | 378 | $A_1(\text{TO})$ |
| $E_1(\text{TO})$ | 410 | 410 | 410 | 410 | | | 409 | 503 | 577 | 410 | $E_1(\text{TO})$ |
| E_2 high | 436 | 437 | 436 | 434 | 435 | | 433 | 517 | 588 | 438 | E_2 high |
| Zn–O disorder | 300–600 440 sh | 520–590 557 max. | 540 | 535 | 537 | 535 | | | | 536 | $2B_1$ low, 2LA |
| $A_1(\text{LO})$ | | 577 | | | 575 | 575 | 584 | 463 | 345 | 574 | $A_1(\text{LO})$ |
| $E_1(\text{LO})$ | | | | | | | 601 | 672 | 735 | 590 | $E_1(\text{LO})$ |
| Zn–O disorder | 655 | 660 | 613, 652 | 649 | 654 | | Observed stretching mode ν | | | | |
| $\nu(\text{O}_2^{2-})$ | 839 | | | | | | 840 (O_2^{2-}) | | | | |
| $\nu(\text{O}-\text{O})$ | 964 | | | | 978 | | | | | 1044, 1072 | TA + LO |
| $\nu(\text{O}_2^-)$ | 1070 | 1110 | 1102 | 1090 | 1085 | | | | | 1105 | TO+LO |
| $\nu(\text{O}_2^-)$ | 1140 | 1138 | 1152 | 1138 | 1140 | | | | | 1158 | 2LO |
| $\nu(\text{O}-\text{O})$ | 1273 | | | | 1269 | | | | | 1150 (O_2^-) | $2A_1(\text{LO}), 2E_1(\text{LO}), 2\text{LO}$ |
| $\nu(\text{O}-\text{O})$ | 1360 | 1350 | | | 1348 | | | | | | |
| $\nu(\text{O}_2)$ | 1570 | 1558 | | | 1520, 1552 | | | | | 1552 (O_2) | |

Note: For comparison, observed bulk ZnO Raman data (very weak bands disregarded)^[30] and observed stretching modes of peroxide^[40] and superoxide^[33] ions in various solids, and of the O_2 molecule^[39] are shown.

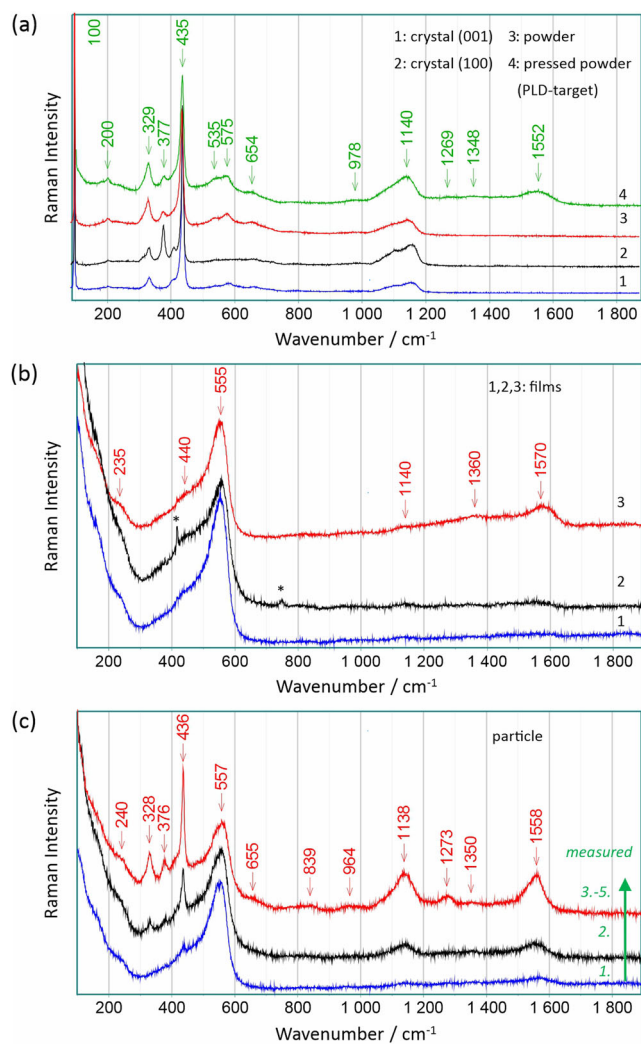


FIGURE 2 (a) Raman spectra of ZnO single crystals (two orientations: (100), (001) \perp to laser beam), powder and pressed powder of the pulsed laser deposition (PLD) target used (arrows indicate assigned wavenumber values of the pressed powder). (b) Raman spectra of three ZnO films (arrows indicate assigned wavenumber values, * bands of the sapphire substrate). (c) Sequence (1., 2., 3–5.) of Raman spectra of a macroscopic ZnO particle (arrows indicate assigned wavenumbers) [Colour figure can be viewed at wileyonlinelibrary.com]

deviation from the principle of strictly corner-connected occupied tetrahedra in ZnO can generate a local inverse occupancy of tetrahedral voids (a filled inversely oriented tetrahedron next to an empty normally oriented tetrahedron), too. Both situations, dioxygen species formation and occupied inverse tetrahedral voids, are illustrated in Figure 3c by the red-colored oxygen atoms. The consequence of this irregular occupancy is an adjustment of the surrounding atoms, which mainly affects the oxygen atoms with short O–O distances (233 pm). Thus, the corresponding oxygen atoms shift to $z \approx 0.5$ to accommodate short O–O distances; compare green-colored oxygen

atoms in Figure 3d. For this case the corresponding Zn–O distances decrease from 198 to 188 pm and the short O–O distances increase from 233 to 275 pm, respectively.

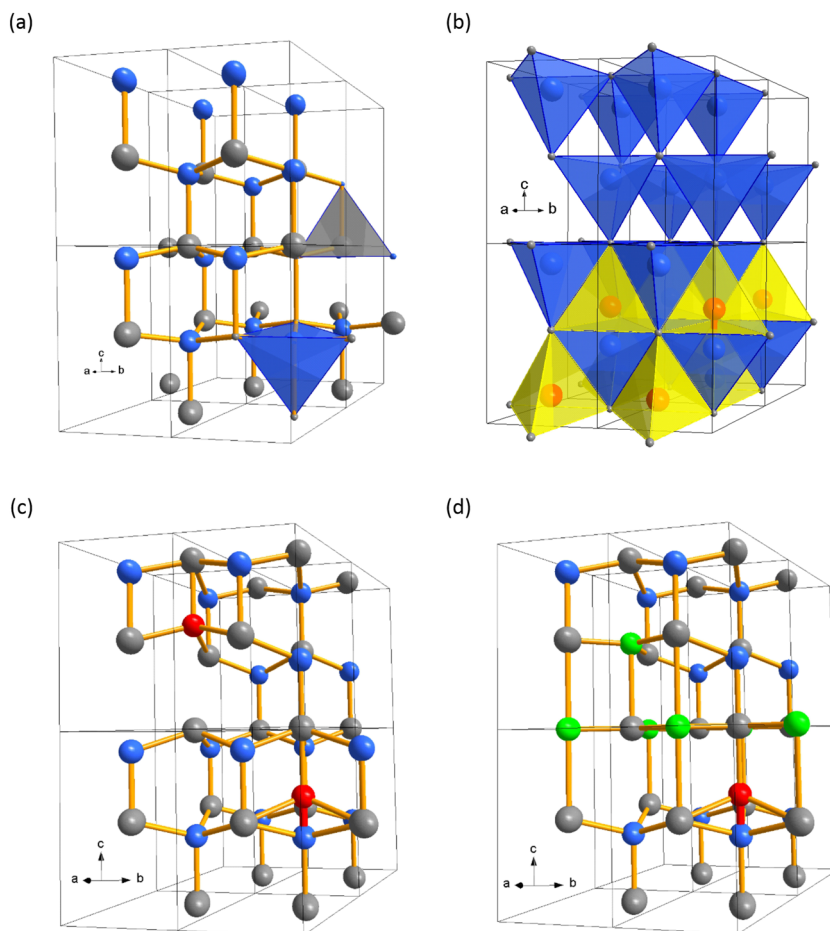
3.3 | Calculated structures

The derived, idealized structural arrangement is verified by DFT calculations using a $2 \times 2 \times 2$ ZnO supercell, where one oxygen ion is replaced by a dioxygen species. Depending on the charge of the dioxygen species, different optimized structures are obtained (see Figure S3 and Table S3). The dioxygen species with two double-negatively charged O^{2-} ions requires a rather large volume (O–O distance 244 pm) accompanied by large displacements of the surrounding atoms. The calculations for lower negative charge (e.g., O_2^{2-} and O_2^-) preserve the dioxygen species with a short O–O distance (154 pm) embedded in a widely intact ZnO lattice. Analogous calculations are performed with one oxygen atom moved from a regular occupied tetrahedral position to an inverse one forming a dioxygen species and an oxygen vacancy. Figure 4a represents this optimized structure, which reveals that both, the oxygen vacancy and the formed dioxygen species (O–O distance 153 pm), are well preserved. The oxygen atoms of the dioxygen species have still the fourfold coordination and the zinc atoms surrounding the oxygen void are threefold coordinated. These results support an unproblematic insertion of these dioxygen species into the ZnO structure. Furthermore, nearly trigonal-planar coordinations are found next to the dioxygen species. This hexagonal planar arrangement (BN structure) is also observed in deposited ZnO monolayers^[35] and is predicted as a possible ZnO crystal structure.^[36]

3.4 | Raman analysis

The displacement of the oxygen position discussed above, where the oxygen atoms shift up to $z \approx 0.5$ (cf. Figure 3d, green-colored oxygen atoms), is only weakly reflected in the intensity variation of the XRD reflections (cf. Figure S4 and Table S2), but strongly influences the Raman spectra. Calculations for the phonon wavenumbers of the ZnO wurtzite structure with the oxygen position at $z = 0.38$, $z = 0.42$, and $z = 0.50$ reveal shifts of the most intensive E_2 -modes from 110 and 433 cm^{-1} to 117 and 517 cm^{-1} , and to 103 and 588 cm^{-1} , respectively (see Table 1). These results suggest a continuous shift of the E_2 -high mode with increasing z -value from 420 to 580 cm^{-1} , which agrees very well with the observed broad band (300 to 600 cm^{-1}) in the Raman spectra of

FIGURE 3 Structural realization of dioxygen species in ZnO. (a) ZnO wurtzite structure ($2 \times 2 \times 2$ supercell, Zn: gray, O: blue); one ZnO_4 (gray) and one OZn_4 tetrahedron (blue). (b) OZn_4 tetrahedra arrangement of wurtzite structure (blue: normally occupied orientation, top-down along c -axis) and partially occupied inversely oriented tetrahedra (yellow: top-up along c -axis, central oxygen atoms red-colored). (c) ZnO wurtzite structure ($2 \times 2 \times 2$ supercell) with one occupied inverse tetrahedron forming the superoxide ion (bottom, red bonding) and one occupied inverse tetrahedron next to an empty normally oriented tetrahedron (top). (d) ZnO wurtzite structure ($2 \times 2 \times 2$ supercell) analogous to (c) with adjusted oxygen atoms (green); compare text. [Colour figure can be viewed at wileyonlinelibrary.com]



the films. The maximum of this band at $\sim 555 \text{ cm}^{-1}$ corresponds to the short Zn–O distances for $z = 0.5$, and all the assumed oxygen positions in-between are represented by the broad shoulder. Additionally, the E_1 and A_1 modes spread from near 600 cm^{-1} to 345 and 735 cm^{-1} for the LO phonons and from near 400 cm^{-1} to 0 and 577 cm^{-1} for the TO phonons. This spreading supports the observed broad spectra of the ZnO films, too.

Additionally, phonon calculations of overall-neutral $2 \times 2 \times 2$ ZnO supercell structures are performed. Figure 4b represents the calculated Raman wavenumbers (brown bars) for the optimized $2 \times 2 \times 2$ ZnO supercell containing a dioxygen species next to an oxygen vacancy (as shown in Figure 4a), overlaid on the Raman spectra of the ZnO film and powder (see also Tables S4 and S5). The calculated wavenumbers reflect the wide ranges of the detected Raman wavenumbers of the ZnO films. Most phonons belong to the broad band from 300 to 600 cm^{-1} as well as to the increasing ramp up to 100 cm^{-1} . Thus, our structural model allows to describe the unexpected Raman spectrum of the deposited ZnO films in an appropriate manner as well as the weak broad bands in the spectrum of ZnO powder. Further remarkable is that the Raman bands at 200 and 330 cm^{-1} of the spectrum of the

ZnO powder are also reproduced by this structure model. Normally, these bands are assigned as double E_2 -high and $(E_2\text{-high})\text{--}(E_2\text{-low})$ modes, respectively.

However, the Raman bands above 700 cm^{-1} , especially the most prominent band at about 1140 cm^{-1} , cannot be explained by the above analysis. In the literature these bands are described as second-order features (overtone/combination) of the ZnO modes. To understand the origin of these bands, it is helpful to consider the deposited macroscopic ZnO particles. The PLD technique generates large particles in the micrometer regime on the substrates, which can be characterized individually by our Raman spectrometer with a laser beam diameter of about $1 \mu\text{m}$. Figure 2c displays a sequence of these measurements taken on the same particle. First, the spectrum of the ZnO particle shows the same broad features as the spectra of the ZnO films combined with a weak E_2 -high mode at 436 cm^{-1} . However, with each measurement on the same particle (second, third, etc.) the spectrum changes, which is not observed for the films. After a few repetitions, a permanent change in the spectrum occurs. Thus, initiated by the irradiation of the Raman laser, the particles order and the expected bulk ZnO vibration modes appear. The spectra of the irradiated ZnO particles

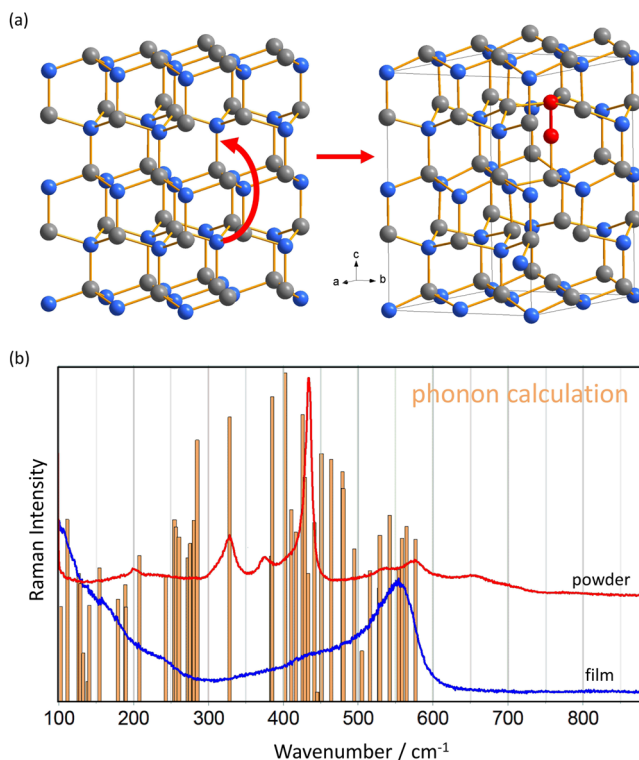


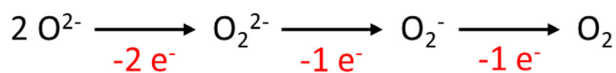
FIGURE 4 (a) Calculated ZnO structures of a $2 \times 2 \times 2$ supercell where one oxygen atom is moved from a regular occupied tetrahedral position to an inverse one (shown left), forming a dioxygen species (red-colored oxygen atoms) and an oxygen vacancy (shown on the right side). (b) Calculated Raman wavenumbers (brown bars, cf. Table S4) of this ZnO $2 \times 2 \times 2$ supercell (as shown in (a) on the right side) compared to Raman spectra of ZnO film (blue spectrum) and powder (red spectrum) [Colour figure can be viewed at wileyonlinelibrary.com]

show Raman bands at 436 (E_2 -high), 410 (E_1 -TO, shoulder), and at 376 (A_1 -TO). The other two expected bands E_1 -LO and A_1 -LO are covered by the broad bands ranging from 520 to 590 cm^{-1} and the E_2 -low modes by the ramp-up to 100 cm^{-1} , which reflect the still existing disorder of the zinc and oxygen atoms. Additionally, the bands at 328, 240, and 655 cm^{-1} can be understood by the structural re-arrangements caused by the dioxygen formation as described above. Furthermore, bands at 839, and 964 cm^{-1} are recorded alongside with the broad bands from 1050 to 1180 cm^{-1} , and previously unreported broad bands at 1273, 1350, and from 1500 to 1600 cm^{-1} (cf. Table 1). In the range from 530 to 700 cm^{-1} Raman bands are ascribed, in the literature, to combinations of optical and acoustic phonons^[30] and are also attributed to defects (oxygen vacancies), displacements, and to electron-phonon interactions, especially in deposited films.^[37,38] The bands at 1050–1180 cm^{-1} are assigned to overtones and combinations of the E_1 -LO and A_1 -LO modes. Here, it is particularly notable that the

strong broad band at 1138 cm^{-1} deviates significantly from the predicted LO bands ($2A_1$: 1148 cm^{-1} , $2E_1$: 1180 cm^{-1})^[35] and is also visible when the first-order LO-bands (574, 590 cm^{-1}) are missing (cf. Figure 2a, spectrum 2). We believe that the origin of all these additional bands above 700 cm^{-1} for ZnO is the presence of dioxygen species in the deposited ZnO films, as discussed below.

First, the band at 1138 cm^{-1} matches very well the symmetric stretching mode of the yellow superoxide ion (O_2^-) with wavenumber values of 1121 to 1164 cm^{-1} determined for the alkali-metal and ammonium superoxides.^[33,34] The broad maxima at around 560 cm^{-1} and the ramp-up to 100 cm^{-1} are the results of the corresponding displaced oxygen and zinc atoms, as described above. Thus, the dioxygen ion generates all these wavenumbers. The Raman spectra of the ZnO powder, pressed powder, and single crystals also show the band at 1140 cm^{-1} , which suggests the presence of superoxides for ZnO in general. Second, the additional band at around 1560 cm^{-1} in the spectra of the films and of the particles is also visible in the spectrum of the pressed powder (PLD target), and this band agrees very well with the stretching mode of the O_2 -molecule of 1552 cm^{-1} .^[39] Thus, it seems possible that both the pressing and our deposition process can stabilize O_2 -molecules inside the ZnO samples, which supports the presence of dioxygen ions, too. We note that the ZnO lattice can very nicely accommodate the O–O distances of O_2 and O_2^- (see above and Figure 3). Third, due to the incorporation of the dioxygen species into the ZnO lattice, the stretching modes of O_2^- and O_2 are broadened. The asymmetric broadening suggests shoulders at 1090 and 1520 cm^{-1} , which can be attributed to different overlapping peaks. The dioxygen species in ZnO can appear in isolation or in groups. These arrangements produce many different coordinations (of Zn by O) and O–O distances, contributing to the variations in the corresponding Raman wavenumbers observed as broadening. Support for the existence of further intermediate distances between O_2 and O_2^- is provided by Raman bands at 1273 and 1360 cm^{-1} and also by the continuously increasing ramp from 800 to 1600 cm^{-1} in the Raman spectra of the ZnO films. The indication, in the measurements, of broad bands between 600 and 1000 cm^{-1} can be explained by dioxygen species with longer O–O distances, for example, by the peroxide ion O_2^{2-} , which shows the stretching mode at 840 cm^{-1} (ZnO_2).^[40] In summary, all observed Raman bands can be explained in a straightforward manner by the presence of dioxygen species inside the ZnO samples.

The asymmetric peak broadening of the band at 1140 cm^{-1} exists also in the spectra of ZnO powder and



SCHEME 1 The formation of dioxygen species creates an excess of negative charge in ZnO. [Colour figure can be viewed at wileyonlinelibrary.com]

especially of single crystals. This can be explained by the presence of domain boundaries consisting of dioxygen species accumulating in an interface layer. This type of superoxide ion interface easily connects the inversely oriented ZnO tetrahedra, as shown in Figure S5. This interface can adjust the domains via the O–O distances, which directly affect the wavenumber of the stretching mode. An analogous structural configuration exists at the basal inversion domain boundaries of doped ZnO samples.^[41,42] Here, the octahedrally coordinated dopants connect the inverted ZnO domains parallel to the (001) lattice plane. Furthermore, the observed color differences of crystal slices cut from single crystals along [001] also support this assumption,^[43] whereby the color reflects different numbers of superoxide ion interfaces per slide.

3.5 | Structure formation procedure

Finally, we demonstrate a scenario for the formation of the atomic arrangement during the ZnO film deposition and inside the macroscopic particles. In our experiments, monoatomic zinc and oxygen, and dioxygen (cf. mass spectra: Figure S6) are ablated from the PLD target and are deposited on the substrate. The effortless charge transfer from zinc to oxygen favors the incorporation of oxygen as O^{2-} ions in the deposited films. With irregular occupancy of the tetrahedral voids by O^{2-} ions, dioxygen species are formed and the observed displacement takes place, as suggested by our theoretical calculations (cf. Figure 4a). Direct incorporation of O_2 -molecules results in a corresponding displacement, too. Additionally, the inserted dioxygen species locally lead to an accumulation of oxygen atoms accompanied by a reduced anion charge, which results in enhanced oxygen defects on regular positions and a (local) excess of negative charge (n-type conductivity); compare Scheme 1.

We believe that the segregation of metallic zinc in our samples is the result of this unbalanced negative charge ($\text{Zn}^{2+} + 2 e^- \rightarrow \text{Zn}$). Thus, highly disordered films are formed with a wide variety of different dioxygen species inside. The detected Raman spectra reflect this structural arrangement. The small crystal sizes of the deposited films support the stability of the disordered films. The macroscopic particles with sizes in the micrometer range

are directly deposited onto the substrate. During this ablation and deposition process, the larger particles disorder, but the atoms remain in quite close contact with each other and can therefore be transformed back into the ordered wurtzite structure by laser irradiation. Zinc and oxygen atoms order to form the tetrahedral network, and mainly superoxide ions and molecular oxygen species are formed, as detected in the Raman spectra. Both dioxygen species fit very well into the ZnO wurtzite structure, which suggests that the occupancy of the inverse tetrahedral voids is an intrinsic structural property of ZnO crystallizing in the wurtzite structure.

4 | CONCLUSION

In conclusion, we present the synthesis of yellow-gray films of ZnO by femtosecond-PLD. The Raman band at 1140 cm^{-1} together with the yellow color support the existence of the superoxide ion O_2^- in our ZnO films as well as in ZnO powders and single crystals, accompanied by the corresponding disordering. Additionally, further dioxygen species are identified, in particular the O_2 -molecule inside the deposited samples and the pressed PLD target. The structural variability is enabled by the flexible ZnO wurtzite structure that tolerates the Zn–O distance variations formed by different displacements. This structural feature is manifested in a small thermal expansion^[44] and the piezoelectricity^[45] of ZnO. The high transparency of the ZnO films^[18] is also a consequence of the disordering. Finally, the insertion of the superoxide ion O_2^- in place of O^{2-} leads to a local excess of negative charge and straightforwardly explains the n-type conductivity^[46] of ZnO as being an intrinsic property.

ACKNOWLEDGEMENTS

D.F. acknowledges the helpful technical support by B. Fenk and U. Waizmann (SEM) at the Max Planck Institute for Solid State Research. D.Z. would like to acknowledge funding by the Ministry of Education, Science, and Technological Development of Serbia (project number 1702201). D.Z. would like to thank Prof. K. Doll, Prof. R. Dovesi, and Crystal Solutions for software support. Open Access funding enabled and organized by Projekt DEAL.

ORCID

Dieter Fischer  <https://orcid.org/0000-0003-2274-9314>

REFERENCES

- [1] H. Moroc, Ü. Özgür, *Zinc oxide: Fundamentals, materials and device technology*, Wiley-VCH, Weinheim 2009, 1.

- [2] J. W. Anthony, R. A. Bideaux, K. W. Bladh, M. C. Nichols, *Handbook of mineralogy*, Vol. 3, Mineral Data Publishing, Tucson **1997**, 624.
- [3] D. Chen, X. Jiao, G. Cheng, *Solid State Commun.* **2000**, *113*, 363.
- [4] F. van Craeynest, W. M. van der Vorst, W. Dekeyser, *Phys. Stat. Sol.* **1965**, *8*, 841.
- [5] D. Ehrentraut, H. Sato, Y. Kagamitani, H. Sato, A. Yoshikawa, T. Fukuda, *Prog. Crystal Growth Charact. Mat.* **2006**, *52*, 280.
- [6] M. Ushio, Y. Sumiyoshi, *J. Mater. Sci.* **1993**, *28*, 218.
- [7] I. A. Kurova, G. M. Kuz'micheva, V. B. Rybakov, *Crystal. Rep.* **2013**, *58*, 226.
- [8] J. Cizek, J. Valenta, P. Hruska, O. Melikhova, I. Prochazka, M. Novotny, J. Bulir, *Appl. Phys. Lett.* **2015**, *106*, 251902.
- [9] D. Ehrentraut, H. Sato, M. Miyamoto, T. Fukuda, M. Nikl, K. Maeda, I. Niikura, *J. Cryst. Growth* **2006**, *287*, 367.
- [10] Ü. Özgür, Y. I. Alivov, C. Liu, A. Teke, M. A. Reshchikov, S. Doğan, V. Avrutin, S.-J. Cho, H. Morkoç, *J. Appl. Phys.* **2005**, *98*, 041301.
- [11] V. Gupta, K. Sreenivas, Pulsed Laser Deposition of Zinc Oxide (ZnO), in *Zinc oxide bulk, thin films and nanostructures*, (Eds: C. Jagadish, S. Pearton), Elsevier, Amsterdam **2006**, 85.
- [12] R. Müller, F. Huber, M. Töws, M. Mangold, M. Madel, J.-P. Scholz, A. Minkow, U. Herr, K. Thonke, *Cryst. Growth des.* **2020**, *20*, 3918.
- [13] Ü. Özgür, V. Avrutin, H. Morkoc, Zinc oxide materials and devices grown by MBE, in *Molecular Beam Epitaxy*, (Ed: M. Henini), Elsevier, Amsterdam **2013** 369.
- [14] N. Sakai, Y. Umeda, F. Mitsugi, T. Ikegami, *Surf. Coat. Technol.* **2008**, *202*, 5467.
- [15] K. Matsubara, P. Fons, K. Iwata, A. Yamada, S. Niki, *Thin Solid Films* **2002**, *422*, 176.
- [16] Y. Inoue, M. Okamoto, T. Kawahara, Y. Okamoto, J. Morimoto, *Mater. Trans.* **2005**, *46*, 1470.
- [17] D. Fischer, A. von Mankowski, A. Ranft, J. Mannhart, B. V. Lotsch, *Chem. Mater.* **2017**, *29*, 5148.
- [18] S. Alhammedi, H. Park, W. K. Kim, *Materials* **2019**, *12*, 1365.
- [19] D. Fischer, B. Andriyevsky, J. C. Schön, *Mater. Res. Express* **2019**, *6*, 116401.
- [20] E. Millon, O. Albert, J. C. Loulergue, J. Etchepare, D. Hulin, W. Seiler, J. Perriere, *J. Appl. Phys.* **2000**, *88*, 6937.
- [21] B. Hadzic, N. Romčević, D. Sibera, U. Narkiewicz, I. Kuryliszyn-Kudelska, W. Dobrowolski, M. Romčević, *J. Phys. Chem. Solid* **2016**, *91*, 80.
- [22] R. Dovesi, A. Erba, R. Orlando, C. M. Zicovich-Wilson, B. Civalleri, L. Maschio, M. Rérat, S. Casassa, J. Baima, S. Salustro, B. Kirtman, *WIREs Comput. Mol. Sci.* **2018**, *8*, e1360.
- [23] F. Pascale, C. M. Zicovich-Wilson, F. L. Gejo, B. Civalleri, R. Orlando, R. Dovesi, *J. Comput. Chem.* **2004**, *25*, 888.
- [24] M. Ferrero, M. Rerat, R. Orlando, R. Dovesi, I. J. Bush, *J. Phys. Conf. Series* **2008**, *117*, 012016.
- [25] A. D. Becke, *J. Chem. Phys.* **1993**, *98*, 5648.
- [26] J. P. Perdew, K. Burke, M. Ernzerhof, *Phys. Rev. Lett.* **1996**, *77*, 3865.
- [27] D. Zagorac, J. C. Schön, J. Zagorac, M. Jansen, *RSC Adv.* **2015**, *5*, 25929.
- [28] R. Hundt, *KPLOT: A program for plotting and Analysing crystal structures*, Technicum Scientific Publishing, Stuttgart **2016**.
- [29] K. Kihara, G. Donnay, *Can. Mineral.* **1985**, *23*, 647.
- [30] R. Cusco, *Phys. Rev. B* **2007**, *75*, 165202.
- [31] H. D. Babcock, *PNAS* **1937**, *23*, 301.
- [32] J. Geurts, *Crystal structure, chemical binding, and lattice*, Springer Series in Materials Science 120 Zinc Oxide, chapter 2, Springer, Berlin **2010** 7.
- [33] W. Hesse, M. Jansen, W. Schnick, *Prog. Solid St. Chem* **1989**, *19*, 47.
- [34] P. D. C. Dietzel, R. K. Kremer, M. Jansen, *J. Am. Chem. Soc.* **2004**, *126*, 4689.
- [35] C. Tusche, H. L. Meyerheim, J. Kirschner, *Phys. Rev. Lett.* **2007**, *99*, 026102.
- [36] D. Zagorac, J. C. Schön, J. Zagorac, M. Jansen, *Phys. Rev. B* **2014**, *89*, 075201.
- [37] V. Russo, M. Ghidelli, P. Gondoni, C. S. Casari, A. Li Bassi, *J. Appl. Phys.* **2014**, *115*, 073508.
- [38] M. Tzolov, *Thin Solid Films* **2000**, *379*, 28.
- [39] D. A. Hatzenbuehler, L. Andrews, *J. Chem. Phys.* **1972**, *56*, 3398.
- [40] D. A. Giannakoudakis, M. Florent, R. Wallace, J. Secor, C. Karwacki, T. J. Bandosz, *Appl Catal B* **2018**, *226*, 429.
- [41] H. Schmidt, E. Okunishi, W. Mader, *Ultramicroscopy* **2013**, *127*, 76.
- [42] V. Ribic, A. Recnik, M. Komelj, A. Kokalj, Z. Brankovic, M. Zlatovic, G. Brankovic, *Acta Mater.* **2020**, *199*, 633.
- [43] M. Suscavage, M. Harris, D. Bliss, P. Yip, S.-Q. Wang, D. Schwall, L. Bouthillette, J. Bailey, M. Callahan, D. C. Look, D. C. Reynolds, R. L. Jones, C. W. Litton, *Mat. Res. Soc. Symp. Proc.* **1999**, *537*, G3.40.
- [44] R. Reeber, *J. Appl. Phys.* **1970**, *41*, 5063.
- [45] Y. Lu, N. W. Emanetoglu, Y. Chen, ZnO Piezoelectric Devices, in *Zinc oxide bulk, thin films and nanostructures*, 1st ed. (Eds: C. Jagadish, S. Pearton), Elsevier, Amsterdam **2006**, 443.
- [46] A. Wang, *Electrical conductivity and doping*, Springer Series in Materials Science 120 Zinc Oxide, chapter 5, Springer, Berlin **2010**, 95.

SUPPORTING INFORMATION

Additional supporting information can be found online in the Supporting Information section at the end of this article.

How to cite this article: D. Fischer, D. Zagorac, J. C. Schön, *J Raman Spectrosc* **2022**, *1*, <https://doi.org/10.1002/jrs.6441>